Chemical Engineering Journal 427 (2022) 130958

Contents lists available at ScienceDirect

Chemical Engineering Journal

journal homepage: www.elsevier.com/locate/cej

Targeting cooling for quantum dots by 57.3°C with air-bubbles-assembled three-dimensional hexagonal boron nitride heat dissipation networks

Bin Xie [a,c], Yujun Wang [a], Haochen Liu [b], Jinlong Ma [a], Shuling Zhou [a], Xingjian Yu [a], Wei Lan [a], Kai Wang [b], Run Hu [a,c,*], Xiaobing Luo [a,c,*]

[a] School of Energy and Power Engineering, Huazhong University of Science and Technology, Wuhan 430074, China
[b] Department of Electrical & Electronic Engineering, Southern University of Science and Technology, Shenzhen 518055, China
[c] Wuhan National Laboratory for Optoelectronics, Huazhong University of Science and Technology, Wuhan 430074, China

ARTICLE INFO

Keywords:
Quantum dots
Light-emitting diodes
Thermal quenching
3D networks
Heat dissipation

ABSTRACT

The non-radiative electron transitions of Quantum dots (QDs) in White light-emitting diodes (WLEDs) not only generates thermal phonons with temperature rise but also degrades their photonic properties. These nanoscale heat sources are usually embedded in low-thermal-conductivity polymer matrix, which is difficult for building efficient heat dissipation pathways without sacrificing the optical performance simultaneously. Herein, we reported an air-bubbles-assembly strategy to construct three-dimensional (3D) thermal dissipation network inside the QDs-WLEDs. Owing to the lateral expulsion of massive microscale air-bubbles, an interconnected hexagonal boron nitride (hBN) network was established under an extremely low hBN loading of 2.74 wt%. With this efficient 3D/hBN network, the highest working temperature of QDs was dramatically decreased by 57.3°C at 700 mA. More than that, the 3D/hBN-WLEDs also show high luminous efficacy of 84.6 lm/W as well as superior color rendering index of Ra = 94.1 and R9 = 93.8, which are comparable to those of traditional WLEDs. The proposed strategy is expected to pave a new door for targeting cooling QDs and other photoluminescent nanoparticles at high-power applications.

1. Introduction

The past few decades have witnessed a significant progress of nanocrystals quantum dots (QDs) in energy-optoelectronic applications such as photovoltaics [1–3], photodetectors [4–6], lasers [7,8], and light-emitting diodes (LEDs) [9–13] due to their extraordinary opto/electronic characteristics like size-dependent bandgaps, wide absorption, narrow emission as well as unique charge-transport properties. In a QD, when electron transits between the discrete energy levels, its energy is released in three ways, namely by emitting photons as radiative process, by giving all energy to other electrons as Auger process, or by transferring energy to both photons and electrons as radiative Auger process [14]. All the non-radiative part of the released energy is converted into thermal phonons and accumulated as heat generation, resulting in a temperature rise of QDs. When QDs' temperature exceeds critical value, significant opto/electronic degradation of QDs has been reported frequently and thus the thermal quenching issue has garnered increasing attentions, especially in high-power applications [15–18].

Recently, QDs are incorporated into the phosphor-converted white LEDs (namely QDs-WLEDs) to supplement the red spectra to improve the light quality for the next generation lighting and display applications [19–25]. Benefited from the facile solution-based synthesis and superior quantum yield (up to 90%) of QDs, the QDs-WLEDs can realize excellent color rendering index (CRI, close to 100) as well as high luminous efficacy (LE) [26–31]. However, the potential application of QDs-WLEDs is severely suppressed by the thermal quenching challenge under high working temperature [32–44]. The thermal quenching of QDs is unavoidable since the thermally induced permanent trap states inside QDs are originated from the intrinsic difference in thermal expansion of the core, shell and ligands materials [35]. These trap states on QDs surface introduce a small energy band near the conduction band of QDs, resulting in irreversible degradation on quantum yields [36]. It has been validated that the working temperature of QDs in high power WLEDs can easily exceed 130°C [36,37], which is significantly beyond the thermal tolerance limitation of commercial QDs and is becoming the bottleneck of QDs-WLEDs in their potential applications.

* Corresponding authors.
E-mail addresses: hurun@hust.edu.cn (R. Hu), luoxb@hust.edu.cn (X. Luo).

https://doi.org/10.1016/j.cej.2021.130958
Received 14 April 2021; Received in revised form 5 June 2021; Accepted 19 June 2021
Available online 23 June 2021

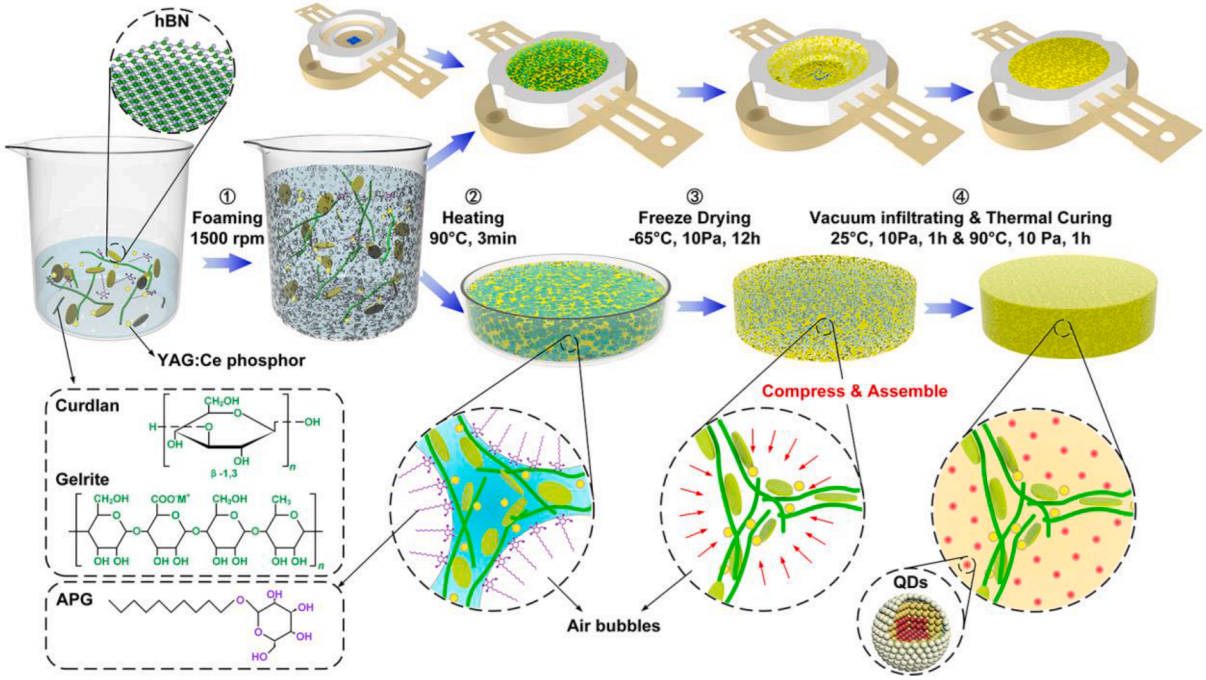

Fig. 1. Schematic of the air-bubbles-assembly method for preparing the 3D/hBN luminescent aerogel and the corresponding 3D/hBN-WLEDs.

Cooling these luminescent nanoparticles is a tough target since they are not only self-heating due to the Stokes loss but also embedded in low-thermal-conductivity polymer matrix. Reinforcing the thermal conductivity of QDs composites seems a direct and effective solution for this thermal issue. But to date, there are few thermally conductive fillers that can be adopted to enhance the thermal conductivity of luminescent composites, because most of reinforcing fillers are light-absorbing materials, such as metals, ceramics and carbon-based composites [38–40], which will deteriorate the optical performance of QDs. Hexagonal boron nitride (hBN), known as 'white graphene', has been demonstrated to be a suitable candidate due to its superior thermal conductivity as well as neglectable absorption of visible light [41,42]. We have validated previously that under a low filler loading of 4.3 wt%, the randomly incorporated hBN platelets successfully enhanced the heat dissipation of QDs/phosphor silicone by reducing the QDs' working temperature as much as 22.7°C [43]. While, when further increasing the hBN filling load, the luminous efficacy of QDs-WLEDs decreased because of the increased scattering and reabsorption energy losses. Therefore, due to the trade-off between light efficiency and heat dissipation performance, the hBN filling load must be restricted to a relatively low range but thereby the cooling capability is limited.

Herein, we report an effective cooling strategy for QDs in WLEDs through establishing three-dimensional (3D) hBN network in the QDs composites. Owing to the lateral expulsion of massive microscale air-bubbles, 3D-interconnected thermal dissipation pathways were established under extremely low fillers fraction. With this efficient 3D/hBN network, the heat generated by QDs and phosphor could be dissipated out quickly, and the light energy could be extracted out efficiently through the porous 3D/hBN structure. Under an extremely low hBN loading of 2.74 wt%, the thermal conductivity of 3D/hBN-luminescent composites reached 0.317 W/(m·K), which is enhanced by 100% compared to the pristine QDs/phosphor silicone. Consequently, the QDs' working temperature in 3D/hBN-WLEDs was dramatically decreased by 57.3°C compared to that in traditional WLEDs under 700 mA illumination, without sacrificing the luminous efficacy.

2. Materials and methods

2.1. Materials

Red-emissive CdSe/ZnS QDs nanocrystals with a peak wavelength of 626 nm and average diameter of 6.8 nm were provided by Poly Opto-Electronics (R-PLQDs, China). High power blue LED modules with rated driving current of 700 mA and peak wavelength of 456 nm were provided by SkyBright (China). Two-component silicone was purchased from Dow Corning (SYLGARD 184, A:B = 10:1). Curdlan and gelrite were purchased from Eonbar Biology (NB-3, China) and Sigma-Aldrich (G1910, low-acyl), respectively, as gelling agents. Alkyl polyglucoside (APG) solution was purchased from Sigma-Aldrich (49122) as a foaming agent. Fig. S1 displays the photograph and SEM image of the hBN platelets. Fig. S2 shows the photographs of phosphor, QDs and blue LED module.

2.2. Preparation of the 3D/hBN-luminescent aerogel

Fig. 1 shows the as-proposed reinforced air-bubbles-assembly method for constructing in-situ 3D/hBN aerogel in WLEDs. Typically, 0.5 ml APG was uniformly dissolved in 25 ml deionized water to form a colorless mixture. Then, 2.5 g hBN platelets, 0.5 g curdlan, 0.3 g gelrite and 1.5 g phosphor powder were added in sequence, followed by a magnetic stirring under 1500 rpm for 30 min. During this process, the hBN and phosphor were uniformly dispersed, and the curdlan/gelrite were dissolved to form a luminescent slurry. Besides, due to the stirring of APG, massive air bubbles were introduced into the slurry, resulting in an obvious volume expansion of the mixture. Next, the slurry was transferred to a 90 °C water bath and stirred at 1000 rpm for another 3–5 min, and then quickly poured into a LED module or other molds. In this heating–cooling process, the hBN platelets and phosphor particles were cross-linked by the curdlan/gelrite molecules, forming a thermally conductive network in the slurry. After cooled down to room temperature, the mixture formed a jelly-like hydrogel due to the solidification of curdlan/gelrite chains. Subsequently, the hydrogel was freeze-dried (Freeze dryer, SCIENTZ-12 N, China) at low temperature (−55°C) and pressure (20 Pa) for 12 h to remove the water molecules and obtain the

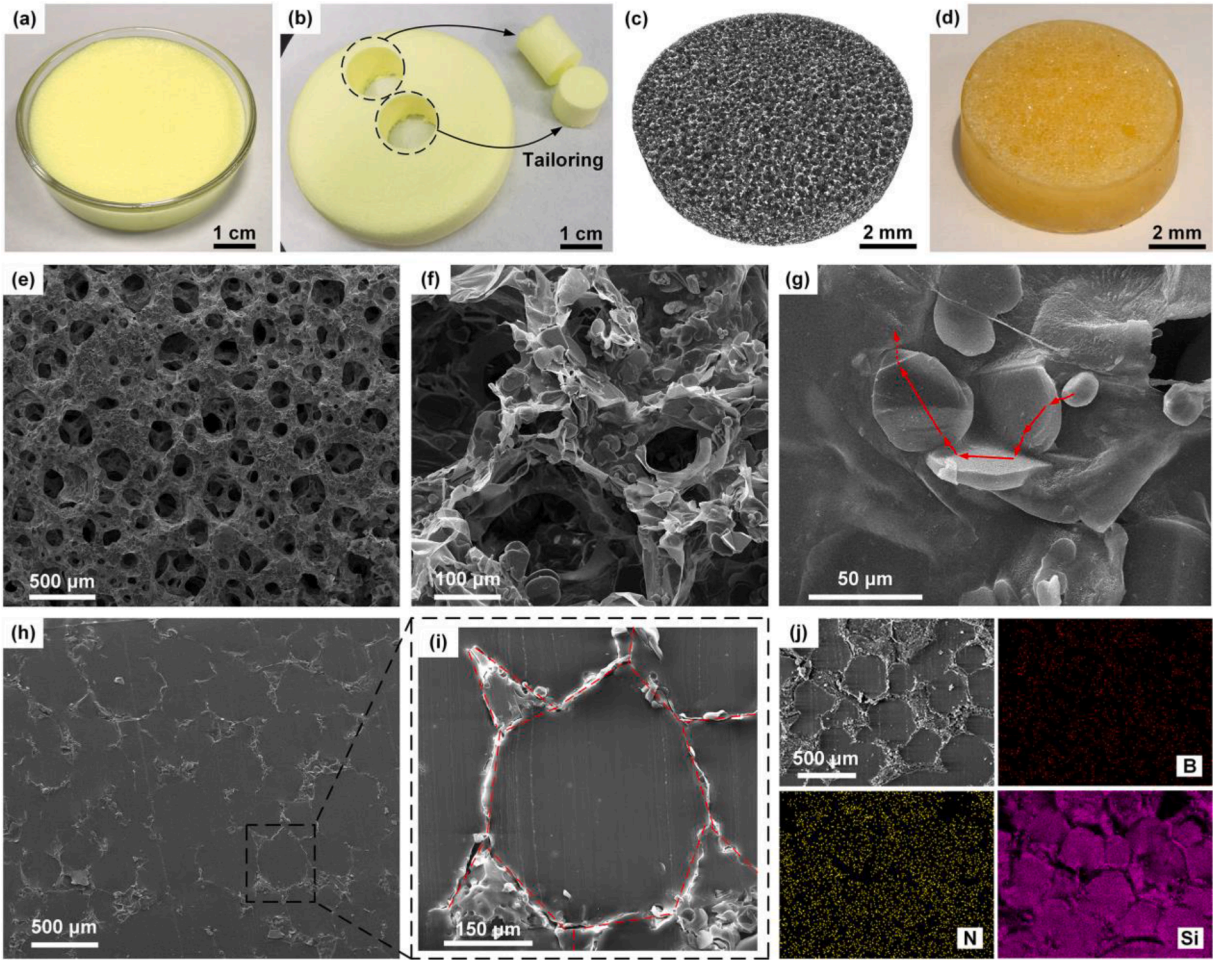

Fig. 2. (a) Photograph of the 3D/hBN-luminescent hydrogels. (b) Photograph of the 3D/hBN-luminescent aerogels. (c) XRT image of the 3D/hBN-luminescent aerogels. (d) Photograph of the 3D/hBN-composites. (e)-(g) SEM images of the 3D/hBN-luminescent aerogels under different magnifications. (h) SEM images of the 3D/hBN-composites. (i) Enlarged view of a local region in (h). (j) SEM image and the corresponding EDS mapping images of the 3D/hBN-composites.

3D/hBN-luminescent aerogel.

2.3. Preparation of 3D/hBN-WLEDs

The silicone and curing agent were first uniformly mixed at room temperature by weight ratio of 10:1. Then, 25 μl QDs-chloroform solution (50 mg/ml) was added into 2 g silicone gel, followed by a vacuum treatment to remove the chloroform and bubbles. Next, the QDs-silicone gel was infiltrated into the as-prepared 3D/hBN-luminescent aerogel of WLEDs under vacuum atmosphere to fill up the voids and obtain the 3D/hBN-composites. Finally, the composites were cured at 90°C for 1 h to obtain the 3D/hBN-WLEDs. As referential samples, the WLEDs with randomly distributed hBN platelets (namely the R/hBN-WLEDs with R/hBN-composites), and traditional WLEDs without hBN platelets (T-WLEDs with T-composites) were also fabricated. For the fabrication of R/hBN-WLEDs, phosphor powder, QDs solution, and same weight fraction of hBN platelets were directly mixed and vacuum-treated to prepare the luminescent composites. Then, the composites were poured into the cavity of blue LED module, followed by a thermal-curing process. For the fabrication of T-WLEDs, the procedures are similar with those of R/hBN-WLEDs, except for the addition of hBN platelets.

2.4. Characterizations

Scanning electron microscope (SEM) images and Energy-dispersive spectroscopy (EDS) mapping images of 3D/hBN-luminescent composites were obtained by a field-emission SEM (Nova NanoSEM 450, FEI) with accelerating voltage of 15 kV. The X-ray tomography (XRT) images of 3D/hBN-luminescent aerogels were obtained by a micro-CT system (skyscan 1172, Bruker). The ultraviolet–visible (UV–VIS) absorption spectra of the QDs and phosphor in the composites were measured by a UV–VIS spectrophotometer (Shimadzu UV-3600). The photoluminescence (PL) spectra and time-resolved PL (TRPL) measurements were carried out in air by a Fluorescence Spectrometers (Edinburgh FLS-980) at a pulse excitation wavelength of 450 nm. The surface temperature of WLEDs samples were obtained by an infrared thermal imager (SC620, FLIR). Thermal diffusivity α of 3D/hBN-luminescent composites was measured through the laser flash method (LFA 457, Netzsch). The test samples were tailored to diameter of 12.7 mm, and a thin graphite film was coated onto their surfaces to avoid laser leakage. Density ρ of the composites were measured by an electron density meter (XF-220SD, LICHEN, China). Specific heat capacity C_p of the composites were measured by a differential scanning calorimetry (Diamond DSC, Perkin Elmer). The thermal conductivity κ of the composites were calculated according to $\kappa = \alpha \cdot C_p \cdot \rho$. The hBN weight fraction in the 3D/hBN-composites were measured by a thermal gravimetric analyzer (Pyris1 TGA, Perkin Elmer). Optical performances of WLEDs were obtained by an integrating sphere system (ATA-1000, Everfine, China). All the optical photographs were taken by a digital camera (Mate 40 Pro, Huawei).

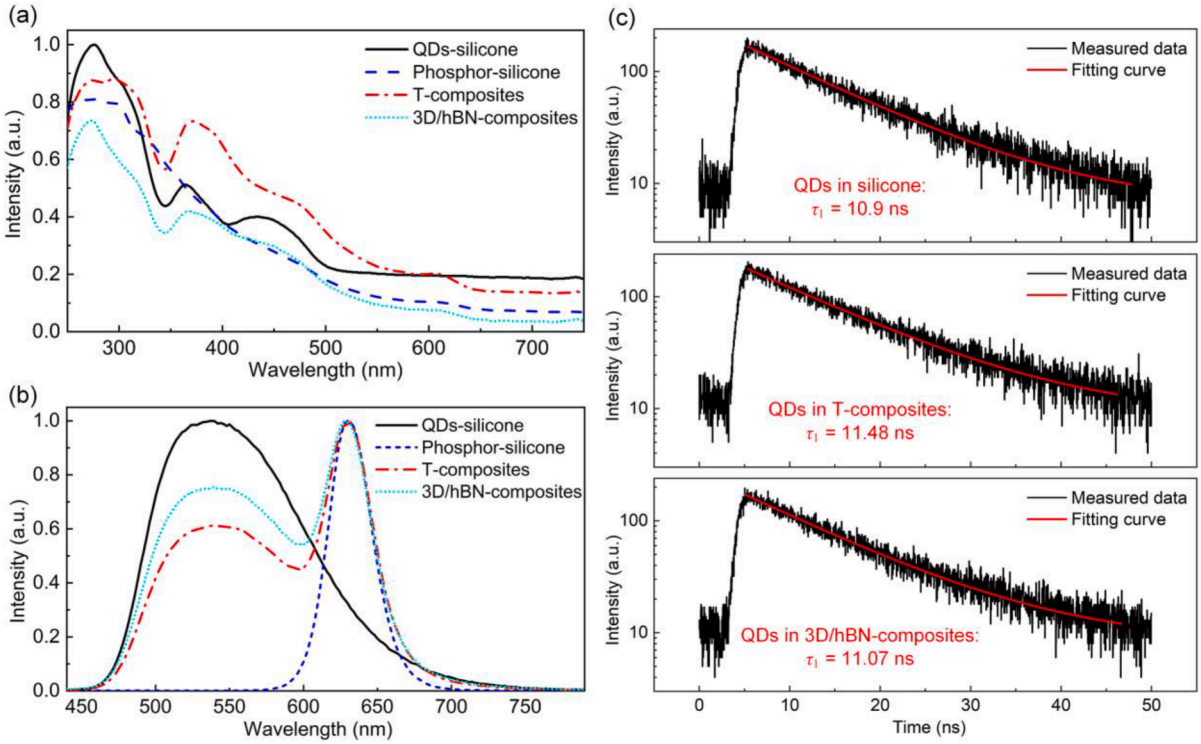

Fig. 3. (a) UV–vis absorption spectra and (b) photoluminescent spectra of QDs-silicone, phosphor-silicone, T-composites and 3D/hBN-composites. (c) TRPL decay curves of QDs in silicone, T-composites and 3D/hBN-composites.

3. Results and discussion

The aim of this work is to build a highly-conductive thermal dissipation network inside the QDs composites without deteriorating the light output performances. For this regard, both efficient interconnections between thermally conductive fillers and expedite escaping channels for photons should be established simultaneously. The air-bubbles-assembly method has been proposed and validated to construct ultralight yet thermally conductive aerogel, like graphene aerogel (GA) [44–46] and hBN aerogel [47]. But GA is not practical since the graphene oxide (GO) gelling agent are strongly absorptive for light. Moreover, according to the bubbles-templated method of preparing hBN aerogel proposed by Li et al. [47], we failed to build a stable hBN aerogel structure under <5 wt% hBN filling fraction, because only the weak shearing force provided by curdlan molecules is insufficient to support the whole network, and the hydrogel would either collapse during the air-dry process or disintegrate during the freeze-dry process.

After persistent trials, we found that gelrite, as another type of bacterial polysaccharide [48], could be cooperated with curdlan to form a reinforced 3D/hBN aerogel under extremely low hBN filling load (~2.5 wt%). Therefore, we proposed a reinforced air-bubbles-assembly method, using both curdlan and gelrite as gelling agents, to prepare the 3D/hBN-luminescent composites and 3D/hBN-WLEDs. As shown in Fig. 1, the hBN platelets, phosphor, curdlan and gelrite powder were firstly dispersed in aqueous solution. Then, the mixture was intensively stirred to dissolve the curdlan and gelrite, and massive air bubbles were generated via the foaming function of APG. In this process, the hBN platelets were excluded by the lateral expulsion of air bubbles, which increase their local aggregations and force them to interconnect with each other. After transferred to a water bath and stirred for several minutes, the slurry was quickly cooled down to room temperature. During this process, the slurry was irreversibly thermal-gelled due to the interconnection between curdlan and gelrite molecules, forming a luminescent hydrogel. The volume of the final hydrogel is several times larger than the original mixture, as shown in Fig. S3, indicating a porous structure has been established.

Fig. 2 displays the photographs and microstructures of the as-prepared 3D/hBN-luminescent hydrogel, 3D/hBN-luminescent aerogel and 3D/hBN-composites. From Fig. 2a and b, it is seen that after freeze-drying process, the 3D/hBN-luminescent aerogel keeps the original shape of hydrogel, which means that the geometry of the aerogel could be conveniently controlled by simply designing the shape of the mold. Fig. 2c, e, and f show the microstructures of the 3D/hBN-luminescent aerogels under different magnification ratios. It is seen from Fig. 2c and e that the massive open pores with diameter of 100 ~ 400 μm were left after the freeze-drying process, forming a 3D interconnected hBN/phosphor network. Fig. 2f and g show the detailed distribution of hBN platelets on the skeleton, from which the continuously connected hBN chains could be observed. Therefore, when the thermal phonons were transferred to the skeleton, they could be dissipated out quickly through the highly thermal-conductive hBN chains, as schematically illustrated in Fig. 2g. Moreover, the abundant open-pores in the 3D/hBN-luminescent aerogel enable light rays to transmit through the whole aerogel. As displayed in Fig. S4, when illuminated by a flashlight from the bottom surface, the aerogel shows a bright and uniform light emission all over the illuminating area. After QDs-silicone infiltration, all the voids in aerogel were filled by the gel, and the as-prepared 3D/hBN-composites show a fully-solid state, as displayed in Fig. 2h. Fig. 2i displays a typical heat dissipation network of the composites, in which the hBN chains connected with each other to form an interconnected spatial network, and the silicone was fully infiltrated into the remaining space. From the Energy dispersive spectroscopy (EDS) mapping images shown in Fig. 2j, the distribution of B, N, and Si elements were clearly illustrated, which confirms the existence of hBN network and the efficient filling of silicone. It should be noted that due to the rare concentration of QDs and phosphor, their distributions were not indicated by the EDS images. To confirm the hBN filling concentration, the thermal gravimetric analysis (TGA) of the 3D/hBN-composites were conducted, and the TGA profiles are shown in Fig. S5. After heated to 600°C, the weight of both pure QDs-silicone gel and 3D/hBN-composites stay stable. The residual mass

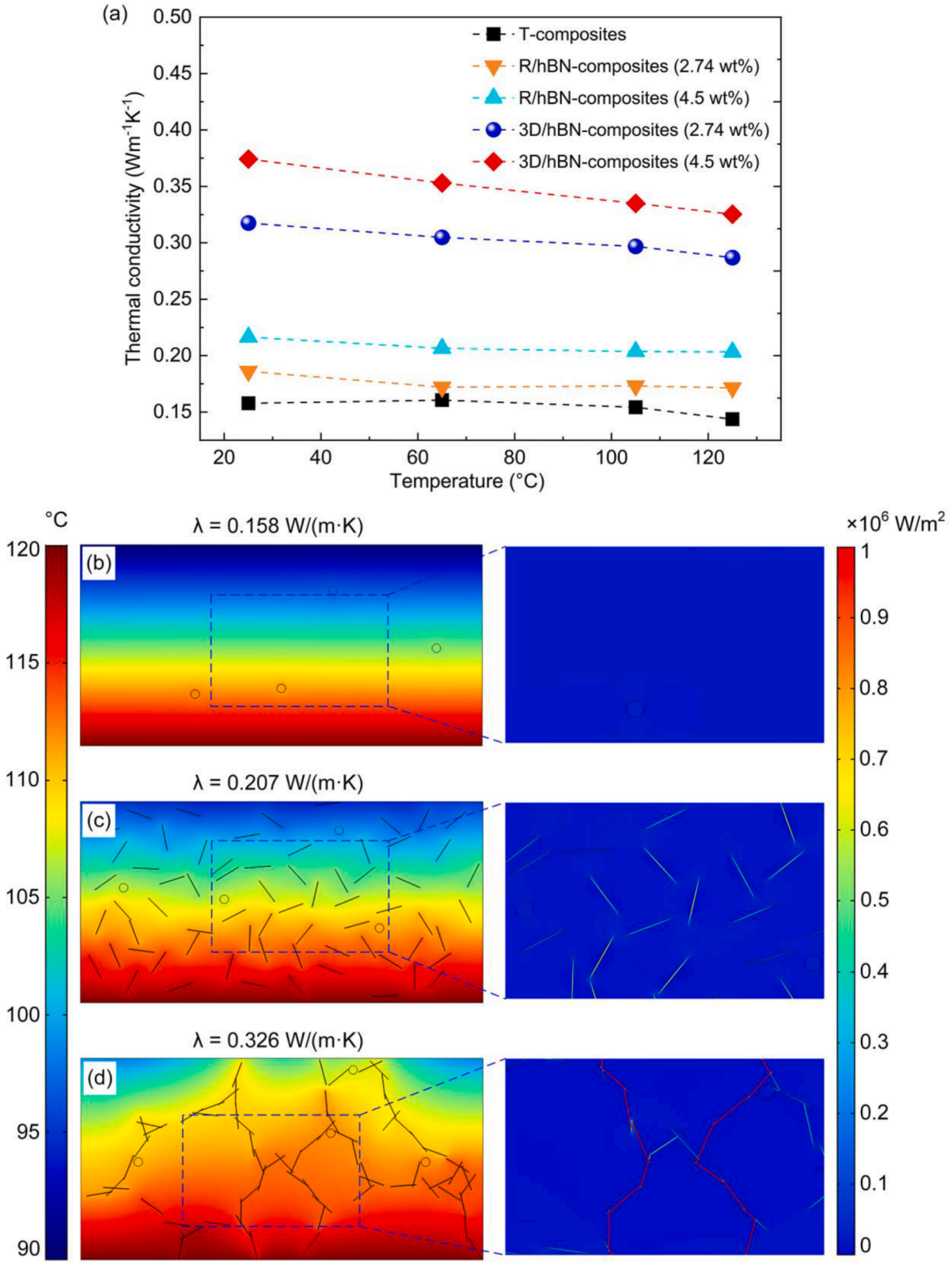

Fig. 4. (a) Measured thermal conductivities of T-composites, R/hBN-composites and 3D/hBN-composites under different ambient temperature. (b)-(d) Simulated temperature and heat flux distributions of the three composites.

fraction of 3D/hBN-composites is 4.38% larger than the pure QDs-silicone gel. This variation is mainly due to the existence of hBN and phosphor. Therefore, according to the original mass ratio of hBN and phosphor (5:3), the hBN filling concentration is calculated as 2.74 wt%.

To investigate the effect of 3D hBN network on the optical response of QDs and phosphor, we measured the UV–VIS absorption spectra and PL spectra of those different composites, as shown in Fig. 3a and b. It is seen that QDs show multiple absorption peaks in silicone, of which the

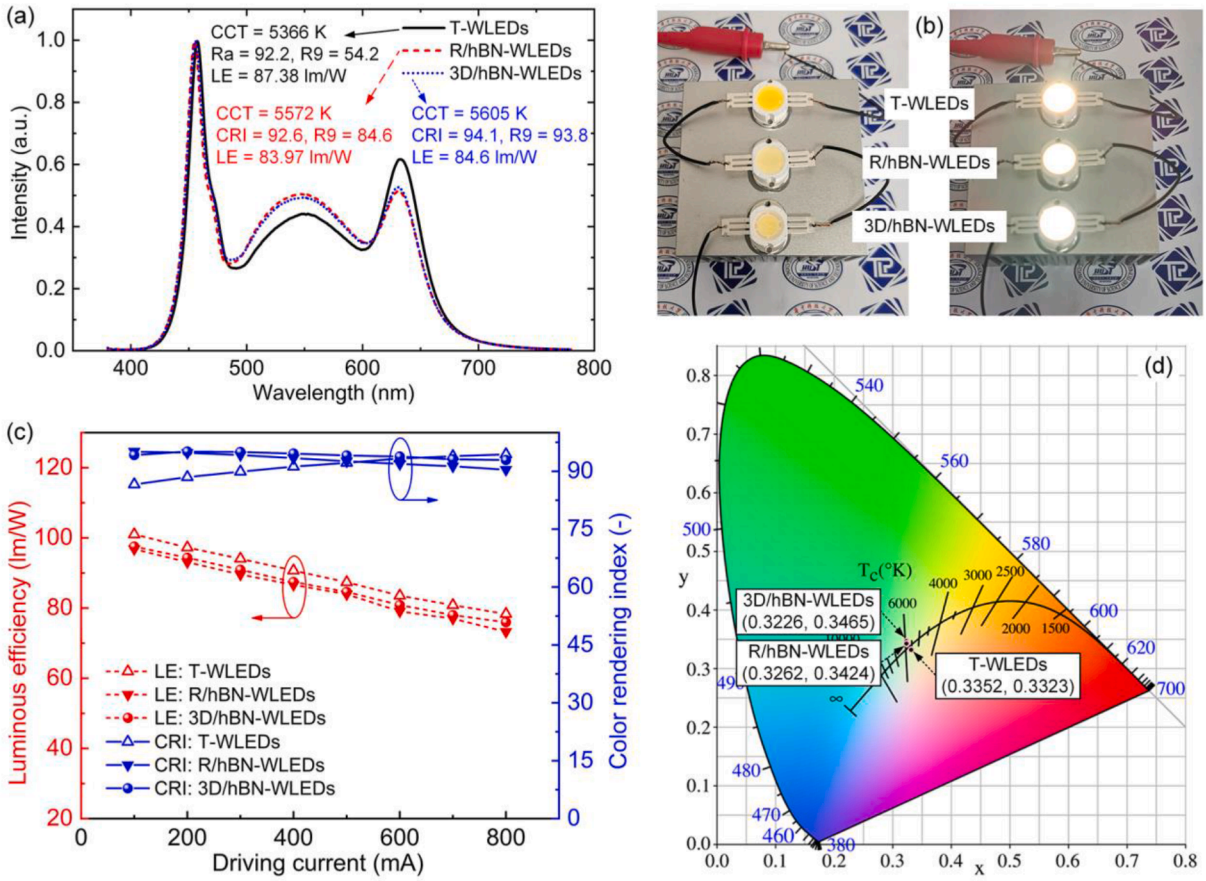

Fig. 5. (a) Spectral power distributions and optical properties of the three kinds of WLEDs under driving current of 500 mA. (b) Photographs of these WLEDs with and without illumination. (c) LE and CRI of the three kinds of WLEDs under different driving currents from 100 to 800 mA. (d) The coordinates of these WLEDs in the CIE 1931 diagram.

highest locates in 280 nm, and the phosphor shows an absorption peak around 300 nm. In the T-composites and 3D/hBN-composites, the absorption peak contributed by QDs is still apparent without evident shift. Moreover, the QDs in different types of composites demonstrate a stable PL spectrum with peak emission wavelength and full-width-at-half-maximum (FWHM) of 630 nm and 34.5 nm, respectively. To further investigate the underlying mechanism of QDs' stability in these different composites, the PL lifetime of QDs in these composites were measured, as shown in Fig. 3c. These TRPL decay curves can be well fitted by an exponential function $I(t) = A_1 e^{-t/\tau 1}$ where $I(t)$ is the PL initial intensity at time t. The PL lifetime of QDs in silicone is calculated as 10.9 ns, and that in T-composites and 3D/hBN-composites is 11.48 ns and 11.07 ns, respectively. The stable PL lifetime of QDs in these composites indicates that there is less energy transfer process took place from QDs donors to hBN acceptors. Therefore, the exist of 3D hBN network has neglectable effect on QDs' optical properties.

Fig. 4a shows the measured thermal conductivities of T-composites, R/hBN-composites, and 3D/hBN-composites with different hBN filling fractions (2.74 wt% and 4.5 wt%). It is seen that the thermal conductivity of T-composites is quite low (0.158 W/(m·K)) due to the intrinsic weak phonon transport ability of unordered polymer chains [49]. More specifically, phonon is the thermal energy carrier in polymer. In the ordered region of polymer, the atoms are in crystalized connect with each other closely and vibrate slightly near equilibrium position, so that the phonon transfers rapidly in the direction of molecule chains. However, in the unordered region of polymer, the crystallinity is not very high due to the random entanglement of the polymer chains, thus the phonons are unable to transport quickly in the unordered region. Besides, the unordered polymer chains also introduce extra boundary scattering towards phonon, resulting in low phonon transport ability. After randomly filled with hBN platelets, the thermal conductivity of the R/hBN-composites shows a limited enhancement, for example, from 0.158 to 0.186 W/(m·K) under hBN filling load of 2.74 wt%. This is mainly because of the relatively low hBN volume fraction which is incapable of forming continuous thermal dissipation channels inside the composites. While, under the same hBN filling fraction, the thermal conductivity of 3D/hBN-composites was significantly reinforced from 0.158 to 0.317 W/(m·K), which is 100% enhanced compared to the T-composites. Besides, when increase the hBN loading to 4.5 wt%, the R/hBN-composites still show a moderate enhancement of thermal conductivity (0.216 W/(m·K)), while the thermal conductivity of the 3D/hBN-composites continues to increase remarkably (0.374 W/(m·K)).

To reveal the underlying heat transfer mechanisms of these three composites, finite element method (FEM) was utilized to simulate the temperature distribution of these composites. The corresponding physical models and boundary conditions were displayed in Fig. S6. Fig. 4b–d shows the simulated temperature and heat flux distributions of the three composites. Concretely, from the FEM results in Fig. 4d, it is seen that due to the existence of air-bubbles, the hBN platelets have higher probability to contact with each other, thus forming an interconnected microstructure. Consequently, the heat flux in these interconnected channels are significantly higher than other region, which confirms the formation of thermal dissipation channels. It is seen that the temperature of top surface in 3D/hBN-composites is obviously higher than that of others, and the T-composites possess a lowest temperature of top surface. Therefore, the heat transfer process from bottom surface to top surface is smoother in the 3D/hBN-composites than in other two composites.

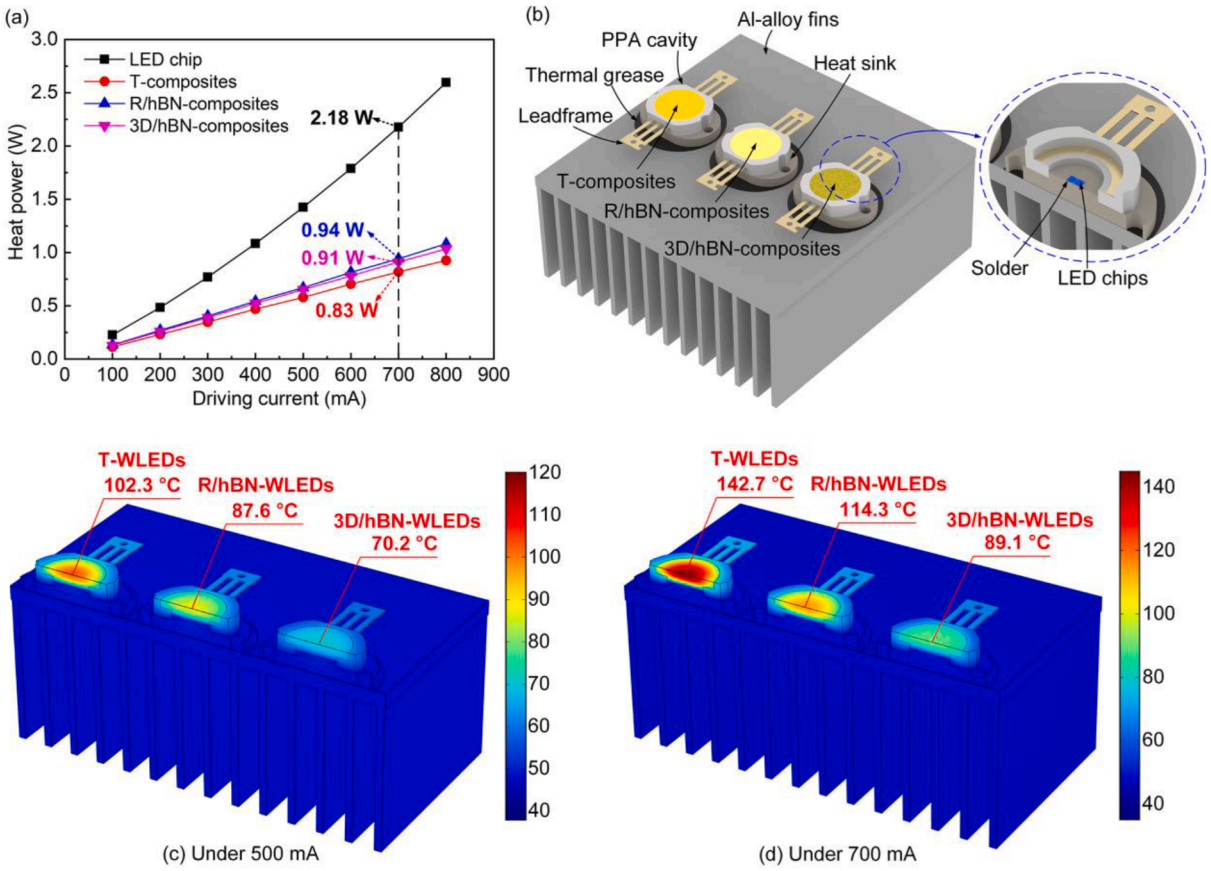

Fig. 6. (a) Measured heat generation in LED chip, T-composites, R/hBN-composites and 3D/hBN-composites under different driving currents from 100 to 800 mA. (b) 3D physical model for the thermal simulation. Simulated temperature distribution of these WLEDs under (c) 500 mA and (d) 700 mA, respectively.

From the corresponding heat flux distributions of these composites, we can see that the heat flux density in hBN platelets is significantly higher than that in silicone, which means that the heat transfer in the composites is mainly relies on hBN. Moreover, the heat flux was severely confined in the isolated hBN platelets of the R/hBN-composites. Therefore, although the phonons transport quickly inside the hBN platelets, they cannot be dissipated out rapidly because the hBN platelets are still surrounded by low-thermal-conductivity silicone. While, in the 3D/hBN composites, continuous hBN chains were formed, thus, the thermal phonons can transport quickly throughout the hBN chains. In other words, the interconnected hBN chains provide efficient escape pathway for the phonons. Consequently, the heat flux density in these continuous hBN chains is an order of magnitude higher than that in isolated hBN platelets. This phenomenon supports the effectiveness of the established 3D interconnected hBN network on heat transfer.

To study the optical performances of the as-prepared 3D/hBN-composites, the corresponding WLEDs (3D/hBN-WLEDs) were fabricated by embedding 3D/hBN-composites into the blue LED module. As references samples, the WLEDs based on T-composites and R/hBN-composites were also prepared, and their correlated color temperature (CCT) were controlled to around 5500 K (neutral white color) by tuning the dosage of QDs/phosphor, and the hBN filling load in the R/hBN-WLEDs and 3D/hBN-WLEDs were controlled as 2.74 wt%. Fig. 5a displays the spectral power distribution of these three WLEDs under the same driving current of 500 mA. It is seen that under similar spectrum, these WLEDs demonstrate high efficiency (LE $>$ 83 lm/W) as well as high color rendering index (CRI $>$ 92), indicating their superior ability to render the true color of objects. Meanwhile, their LE performances were quite close (within deviation of 4%), which means that this low hBN filling load contributes neglectable effect to the light output efficiency of WLEDs. To further investigate the light transmittance and conversion process in the three composites, the transmittance of blue light as well as the conversion ratio of yellow and red light in these WLEDs were calculated according to the measured data, as shown in Fig. S7. It is seen that about 15% of the total blue light energy was transmitted from the composites, and about 40% is converted into yellow and red light by phosphor and QDs, respectively. Thus, about 45% of the total blue light is converted into heat power. Moreover, the transmittance and conversion ratio among these WLEDs vary insignificantly (less than 2%), which also indicates the neglectable influence of 3D/hBN network to the optical properties of WLEDs. Fig. 5b displays the photographs of these WLEDs with and without illumination, which clearly demonstrate the comparable appearance and optical performance of 3D/hBN-WLEDs. Fig. 5c shows their LE and CRI variation under different driving currents from 100 to 800 mA. From the results, we can see that the CRI of these WLEDs remain stable with the increasing driving current, suggesting their consistent color rendering ability under various lighting conditions. Meanwhile, these WLEDs demonstrate similar trends of LE drop under increasing driving current. This is mainly because of the efficiency drop of LED chip itself under crowded electron-hole pairs [50]. Fig. 5d indicates the location of these WLEDs in the CIE 1931 diagram. It is seen that they are quite close to the central region of Planck blackbody curve, indicating a neutral, high quality white light illumination. Additionally, we also measured the optical properties of the 3D/hBN-WLEDs which contains 4.5 wt% of hBN platelets. The results indicate that the LE was decreased to 76.6 lm/W due to the overload of hBN platelets which obstruct the light output from the composites. Based on above results, it is validated that the construction of 3D/hBN aerogel in WLEDs does not causes evident efficiency drops under an optimized hBN filling load.

To study the thermal performances of the as-prepared 3D/hBN-WLEDs, the heat power generated in LED chip, T-composites, R/hBN-

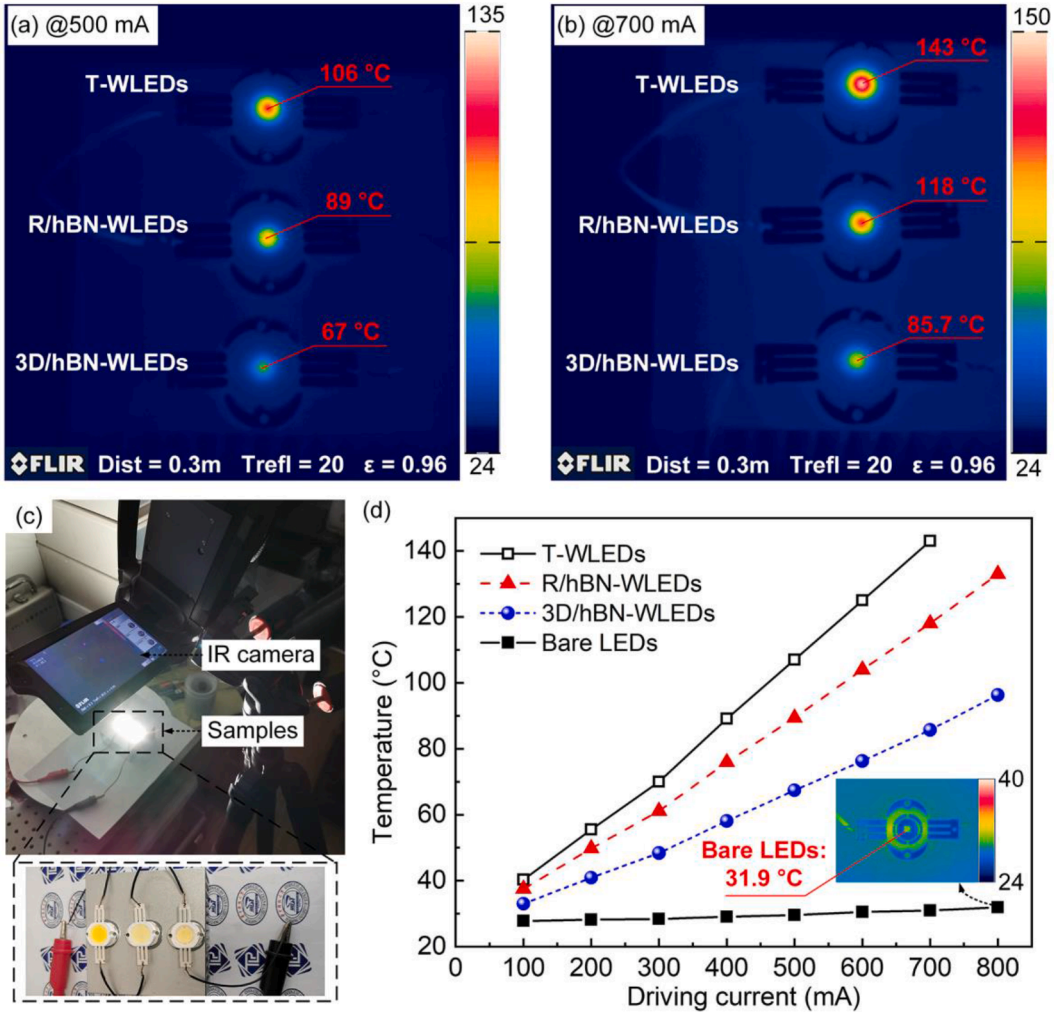

Fig. 7. Measured surface temperature distributions of the three WLEDs under driving current of (a) 500 mA and (b) 700 mA, respectively. (c) Temperature measurement setup. The lower figure shows the zoomed photograph of these WLEDs in the current-off status. (d) Measured highest surface temperature of the three WLEDs under different driving currents from 100 to 800 mA. The inset shows the surface temperature of bare LEDs under driving current of 800 mA.

composites and 3D/hBN-composites were measured and calculated according to the energy conservation law [51,52]. The measured heat power is illustrated in Fig. 6a. From the results, we can see that the LED chip generates much heat then those luminescent composites, especially under higher driving current. For instance, the heat power of LED chip is 2.18 W under 700 mA, which is over two times as those in the composites (less than 1 W). In addition, the heat generation in T-composites, R/hBN-composites and 3D/hBN-composites are quite close, which also proves that the introduce of 3D/hBN aerogel does not cause extra heat generation to the composites.

Based on the measured heat power results, the steady-state temperature distributions of these three WLEDs were simulated. The physical model is illustrated in Fig. 6b (see supporting information for the detailed simulation setup), and the results are displayed in Fig. 6c and d. It is seen that thanks to the robust heat conduction ability of Al-alloy fins, most of the heat was dissipated out to ambient air. While, due to the low thermal conductivity of the T-composites, the heat generated by QDs/phosphor was confined and accumulated inside the composites, resulting in a high working temperature of 102.3°C under 500 mA. After incorporating R/hBN into the WLEDs, the highest working temperature was reduced to 87.6°C. By constructing 3D/hBN network inside the WLEDs, the highest working temperature was further decreased to 70.2°C. Furthermore, under a higher driving current of 700 mA, situation of QDs in the T-WLEDs turns worse with a highest temperature of 142.7°C, while the QDs in the 3D/hBN-WLEDs stay cool with a highest temperature of 89.1°C. Therefore, the results clearly demonstrate the effectiveness of 3D/hBN network on the temperature reduction of WLEDs, especially under high power condition.

To validate the simulation results, we also measured the surface temperature distributions of these WLEDs under 500 mA and 700 mA by an infrared thermal imager, as displayed in Fig. 7a and b, respectively. These WLEDs were mounted onto an Al-alloy fins by thermal grease, and they are connected in series by electrical wires to make sure that they are in the same working condition, as shown in Fig. 7c. The surface emissivity of the composites is set as 0.96, and the testing distance between the camera and these WLEDs is controlled as 0.3 m. Their surface temperature distributions were recorded after the temperature variation of each WLEDs is less than 1% within 3 min, which took about 3 min since the WLEDs were lighted up (Fig. S8 shows the monitored temperature rising process of these WLEDs under 700 mA driven). From the measured temperature distributions, it is seen that the experimental results have verified the FEM simulation results, and the maximum error of highest working temperature is less than 5%. Under 700 mA, the measured highest working temperature of WLEDs is reduced by 57.3°C by the proposed 3D/hBN aerogel. Besides, it can be observed from Fig. 7d that the temperature reduction is more apparent under higher driving current. Moreover, under the same working condition, the measured surface temperature of bare LEDs (without luminescent

composites) in Fig. 7d is significantly lower than those WLEDs with luminescent composites. This is mainly due to the good heat dissipation environment of LED chips that are directly contacted with the metal heat sink and Al-alloy fins. Therefore, both the simulated and measured results have demonstrated that the heat dissipation bottleneck in WLEDs is the low-thermal-conductivity luminescent composites, and the utilization of 3D/hBN aerogel is effective in reinforcing the thermal dissipation luminescent composites, thus solving the thermal dissipation challenge of WLEDs. Because of the decreased working temperature, the long-term stability of QDs is supposed to be enhanced. Therefore, QDs-LEDs samples which consist of LED chip and QDs-silicone (labeled as T-LEDs), and QDs-LEDs samples which consist of LED chip and 3D/hBN-QDs-silicone (labeled as 3D/hBN-LEDs) were fabricated to directly validate the benefit of 3D/hBN network towards QDs stability. Their color coordinates were controlled at around (0.34, 0.13) by slightly tuning the QDs dosage. Then, they are mounted onto an Al-alloy substrate for long-term aging test under driving current of 200 mA, and the PL intensity of QDs was monitored every 24 h. Before aging, the highest working temperature of QDs in the T-LEDs and 3D/hBN-LEDs was measured as 100.3°C and 82.9°C, respectively. Fig. S9 shows the relative PL decay curves of these samples. It is seen that after 168 h, 63% of the original PL intensity is still retained in the 3D/hBN-LEDs, while that in the T-LEDs only retains 38%. In addition, it is clearly seen from their illumination pattern that the T-LEDs lost majority of red emission after 168 h, and their color coordinates shifted to (0.2482, 0.0902), while the 3D/hBN-LEDs only shifted to (0.2946, 0.1127). The aging test has directly proved that the QDs stability can be enhanced by reinforcing their thermal dissipation through the 3D/hBN network.

4. Conclusions

QDs are not only self-heating but also embedded in low-thermal-conductivity silicone gel, cooling QDs is rather challenging especially in high-power WLEDs. To solve this issue, we reported an effective strategy with air-bubbles-assembly method to construct 3D/hBN thermal dissipation networks inside the WLEDs. Both optical properties and thermal performances of the 3D/hBN-WLEDs were characterized. Thanks to the efficient heat dissipation network, the heat generated by QDs and phosphor could be dissipated out quickly, and the light rays could escape smoothly through the highly porous 3D/hBN structure. Under an extremely low hBN loading of 2.74 wt%, the thermal conductivity of the 3D/hBN-luminescent composites reached 0.317 W/(m·K), which is 100% enhancement compared to the pristine QDs/phosphor silicone. Consequently, the highest working temperature in 3D/hBN-WLEDs was dramatically decreased by 57.3°C compared to that in traditional WLEDs under 700 mA, without sacrificing the luminous efficacy. The proposed method is expected to remove the thermal barrier in the way of high power QDs-WLEDs applications.

Declaration of Competing Interest

The authors declare that they have no known competing financial interests or personal relationships that could have appeared to influence the work reported in this paper.

Acknowledgements

This work is supported by the National Natural Science Foundation of China(51625601, 52076087), China Postdoctoral Science Foundation (2021M693108), the Ministry of Science and Technology of the People's Republic of China (2017YFE0100600), the financial support from Creative Research Groups Funding of Hubei Province (2018CFA001), the Open Project Program of Wuhan National Laboratory for Optoelectronics (2018WNLOKF017) and Postdoctoral Creative Research Funding of Hubei Province.

Appendix A. Supplementary data

Supplementary data to this article can be found online at https://doi.org/10.1016/j.cej.2021.130958.

References

[1] O.E. Semonin, J.M. Luther, S. Choi, H.Y. Chen, J. Gao, A.J. Nozik, M.C. Beard, Science 334 (2011) 1530–1533.
[2] C.H.M. Chuang, P.R. Brown, V. Bulovic, M.G. Bawendi, Nat. Mater. 13 (2014) 796–801.
[3] X. Li, J. Yu, J. Low, Y. Fang, J. Xiao, X. Chen, J. Mater. Chem. A 3 (2015) 2485–2534.
[4] L. Dou, Y. Yang, J. You, Z. Hong, W.H. Chang, G. Li, Y. Yang, Nat. Commun. 5 (2014) 5404.
[5] L. Su, Z.X. Zhao, H.Y. Li, J. Yuan, Z.L. Wang, G.Z. Cao, G. Zhu, ACS Nano 9 (2015) 11310–11316.
[6] X. Liu, X. Ji, M. Liu, N. Liu, Z. Tao, Q. Dao, L. Wei, C. Li, X. Zhang, B. Wang, A.C. S. Appl, Mater. Inter. 7 (2015) 2452–2458.
[7] Y. Fu, H. Zhu, C.C. Stoumpos, Q. Ding, J. Wang, M.G. Kanatzidis, X. Zhu, S. Jin, ACS Nano 10 (2016) 7963–7972.
[8] G. Xing, N. Mathews, S.S. Lim, N. Yantara, X. Liu, D. Sabba, M. Gratzel, S. Mhaisalkar, T.C. Sum, Nat. Mater. 13 (2014) 476–480.
[9] Y. Shirasaki, G.J. Supran, M.G. Bawendi, V. Bulovic, Nat. Photonics 7 (2013) 13–23.
[10] J. Song, J. Li, X. Li, L. Xu, Y. Dong, H. Zeng, Adv. Mater. 27 (2015) 7162–7167.
[11] T.H. Le, Y. Choi, S. Kim, U. Lee, E. Heo, H. Lee, S. Chae, W.B. Im, H. Yoon, Adv. Opt. Mater. 8 (2020) 1901972.
[12] X. Hu, J. Liu, X. Du, R. Cheng, Q. Li, S. Chen, J. Mater. Chem. C 7 (2019) 10988–10995.
[13] J. Wang, F. Tang, Y. Wang, S. Liu, L. Li, Adv. Opt. Mater. 8 (2020) 1901571.
[14] H.S. Jang, H. Yang, S.W. Kim, J.Y. Han, S.G. Lee, D.Y. Jeon, Adv. Mater. 20 (2008) 2696–2702.
[15] Y. Zhao, C. Riemersma, F. Pietra, R. Koole, C.D. Donega, A. Meijerink, ACS Nano 6 (2012) 9058–9067.
[16] F. Gao, W. Yang, X. Liu, Y. Li, W. Liu, H. Xu, Y. Liu, Chem. Eng. J. 407 (2021), 128001.
[17] W. Yang, F. Gao, Y. Qiu, W. Liu, H. Xu, L. Yang, Y. Liu, Adv. Opt. Mater. 7 (2019) 1900546.
[18] W. Yang, L. Fei, F. Gao, W. Liu, H. Xu, L. Yang, Y. Liu, Chem. Eng. J. 387 (2020), 124180.
[19] W. Chung, H.J. Yu, S.H. Park, B.H. Chun, S.H. Kim, Mater. Chem. Phys. 126 (2011) 162–166.
[20] X. Dai, Z. Zhang, Y. Jin, Y. Niu, H. Cao, X. Liang, L. Chen, J. Wang, X. Peng, Nature 515 (2014) 96–99.
[21] F. Zhang, H. Zhong, C. Chen, X. Wu, X. Hu, H. Huang, J. Han, B. Zou, Y. Dong, ACS Nano 9 (2015) 4533–4542.
[22] J. Li, L. Xu, T. Wang, J. Song, J. Chen, J. Xue, Y. Dong, B. Cai, Q. Shan, B. Han, H. Zeng, Adv. Mater. 29 (2017) 1603885.
[23] E. Jang, S. Jun, H. Jang, J. Llim, B. Kim, Y. Kim, Adv. Mater. 22 (2010) 3076–3080.
[24] X. Wang, S. Yan, W. Li, K. Sun, Adv. Mater. 24 (2012) 2742–2747.
[25] A. Aboulaich, M. Michalska, R. Schneider, A. Potdevin, J. Deschamps, R. Deloncle, G. Chadeyron, R. Mahiou, ACS Appl. Mater. Inter. 6 (2014) 252–258.
[26] B. Chen, Q. Zhou, J. Li, F. Zhang, R. Liu, H. Zhong, B. Zou, Opt. Express 21 (2013) 10105–10110.
[27] B. Xie, R. Hu, X. Luo, J. Electron. Packaging 138 (2016), 020803.
[28] W.S. Song, H. Yang, Chem. Mater. 24 (2012) 1961–1967.
[29] Z. Wang, F. Yuan, X. Li, Y. Li, H. Zhong, L. Fan, S. Yang, Adv. Mater. 29 (2017) 1702910.
[30] T. Erdem, S. Nizamoglu, X.W. Sun, H.V. Demir, Opt. Express 18 (2010) 340–347.
[31] H.C. Yoon, H. Kang, S. Lee, J.H. Oh, H. Yang, Y.R. Do, ACS Appl. Mater. Inter. 8 (2016) 18189–18200.
[32] P.H.C. Camargo, Y.H. Lee, U. Jeong, Z.Q. Zou, Y.N. Xia, Langmuir 23 (2007) 2985–2992.
[33] K. Miszta, D. Dorfs, A. Genovese, M.R. Kim, L. Manna, ACS Nano 5 (2011) 7176–7183.
[34] B. Xie, Y. Cheng, J. Hao, X. Yu, W. Shu, K. Wang, X. Luo, IEEE T. Electron Dev. 65 (2018) 605–609.
[35] J.H. Jo, M.S. Kim, C.Y. Han, E.P. Jang, Y.R. Do, H. Yang, Appl. Surf. Sci. 428 (2018) 906–911.
[36] Z. Li, Y. Chen, J. Li, S. Liang, Y. Tang, Appl. Therm. Eng. 179 (2020), 115666.
[37] Y. Peng, Y. Mou, T. Wang, H. Wang, R. Liang, X. Wang, M. Chen, X. Luo, IEEE T. Electron Dev. 66 (2019) 2637–2642.
[38] G. Lian, C.C. Tuan, L. Li, S. Jiao, Q. Wang, K.S. Moon, D. Cui, C.P. Wong, Chem. Mater. 28 (2016) 6096–6104.
[39] M. Wang, H. Chen, W. Lin, Z. Li, Q. Li, M. Chen, F. Meng, Y. Xing, Y. Yao, C. P. Wong, Q. Li, ACS Appl. Mater. Inter. 6 (2014) 539–544.
[40] V. Goyal, A.A. Balandin, Appl. Phys. Lett. 100 (2012), 073113.
[41] J. Wang, D. Liu, Q. Li, C. Chen, Z. Chen, P. Song, J. Hao, Y. Li, S. Fakhrhoseini, M. Naebe, X. Wang, W. Lei, ACS Nano 13 (2019) 7860–7870.
[42] H. Fang, S. Bai, C.P. Wong, Compos. Commun. 2 (2016) 19–24.
[43] B. Xie, H. Liu, R. Hu, C. Wang, J. Hao, K. Wang, X. Luo, Adv. Funct. Mater. 28 (2018) 1801407.

[44] H. Yang, Z. Li, B. Lu, J. Gao, X. Jin, G. Sun, G. Zhang, P. Zhang, L. Qu, ACS Nano 12 (2018) 11407–11416.
[45] X. Zhang, T. Zhang, Z. Wang, Z. Ren, S. Yan, Y. Duan, J. Zhang, ACS Appl.Mater. Inter. 11 (2019) 1303–1310.
[46] L. Lv, P. Zhang, H. Cheng, Y. Zhao, Z. Zhang, G. Shi, L. Qu, Small 12 (2016) 3229–3234.
[47] J. Li, F. Li, X. Zhao, W. Zhang, S. Li, Y. Lu, L. Zhang, ACS Appl. Electronic Mater. 2 (2020) 1661–1669.
[48] M. Aslam, S.S. Imam, M. Aqil, Y. Sultana, A. Ali, J. Polym. Eng. 36 (2016) 761–769.
[49] Y. Xu, D. Kraemer, B. Song, Z. Jiang, J. Zhou, J. Loomis, J. Wang, M. Li, H. Ghasemi, X. Huang, X. Li, G. Chen, Nat. Commun. 10 (2019) 1771.
[50] A.V. Zinovchuk, O.Y. Malyutenko, W.K. Malyutenko, A.D. Podoltsev, A.A. Vilisov, J. Appl. Phys. 104 (2008), 033115.
[51] Y. Xie, D. Yang, L. Zhang, Z. Zhang, C. Geng, C. Shen, J.G. Liu, S. Xu, W. Bi, ACS Appl. Mater. Inter. 12 (2020) 1539–1548.
[52] B. Xie, W. Chen, J. Hao, D. Wu, X. Yu, Y. Chen, R. Hu, K. Wang, X. Luo, Opt. Express 24 (2016) A1560–A1570.